Review of Scientific Instruments ARTICLE scitation.org/journal/rsi

Extension of charged-particle spectrometer capabilities for diagnosing implosions on OMEGA, Z, and the NIF

Cite as: Rev. Sci. Instrum. 92, 083506 (2021); doi: 10.1063/5.0062584
Submitted: 6 July 2021 • Accepted: 23 July 2021 •
Published Online: 5 August 2021

B. Lahmann,[a] M. Gatu Johnson, J. A. Frenje, A. J. Birkel, P. J. Adrian, N. Kabadi, J. H. Kunimune, T. M. Johnson, J. A. Pearcy, B. L. Reichelt, F. H. Séguin, G. Sutcliffe, and R. D. Petrasso

AFFILIATIONS

Massachusetts Institute of Technology, Cambridge, Massachusetts 02139, USA

[a]Author to whom correspondence should be addressed: lahmann@mit.edu

ABSTRACT

New designs and a new analysis technique have been developed for an existing compact charged-particle spectrometer on the NIF and OMEGA. The new analysis technique extends the capabilities of this diagnostic to measure arbitrarily shaped ion spectra down to 1 MeV with yields as low as 10^6. Three different designs are provided optimized for the measurement of DD protons, T^3He deuterons, and $^3He^3He$ protons. The designs are highly customizable, and a generalized framework is provided for optimizing the design for alternative applications. Additionally, the understanding of the detector's response and uncertainties is greatly expanded upon. A new calibration procedure is also developed to increase the precision of the measurements.

I. INTRODUCTION

Measuring charged-particle spectra is of great importance to both inertial confinement fusion (ICF) and high-energy-density-physics (HEDP) experiments on the NIF[1] and OMEGA[2] laser facilities. It is also crucial for neutron-recoil spectrometers because they infer neutron spectra directly from the measurement of charged-particle spectra.[3–5] This expands the relevance to the Z facility[6] where neutron-recoil spectrometers are projected to be implemented.[5] From both neutron and charged-particle spectra, one can infer various plasma properties, such as areal density (ρR), ion temperatures (T_{ion}), or asymmetries.[7–12] Over decades, several CR-39 based spectrometers have been developed and fielded on all three facilities for this reason.[3,9–13] Among these are the step range filters (SRFs), originally designed specifically for measuring fusion protons from DD reactions,[12]

$$D + D \rightarrow T(1.01\,MeV) + p(3.02\,MeV). \quad (1)$$

The SRFs have an important role at the NIF and OMEGA due to their unique coverage range of low yields and low energies. Figure 1 shows the entire coverage of the SRFs and other charged-particle diagnostics for protons on both facilities. In addition to this, the SRFs are a non-fixed diagnostic with a highly simplistic design. This makes it possible to field roughly 20 per experiment on both NIF and OMEGA, each in different locations around the experiment.

The SRFs will also play an important role on the Z facility through a new non-magnetic neutron-recoil spectrometer which has recently been developed.[5] This spectrometer infers a neutron spectrum from the measurement of low-energy (<4 MeV) elastically scattered protons. Because the system is non-magnetic, this measurement can only be accomplished using an SRF again due to the low particle energies.

While important, SRFs have had a handful of limitations in their early iterations. Early designs had limited energy coverage (1–3 MeV) and the analysis used on them only worked for Gaussian shaped DD-proton spectra.[12] In this work, a new design geometry has been developed with multiple advantages over previous designs. This new design extends the energy coverage of a given SRF while also minimizing calibration complexity. Additionally, a new analysis technique has been developed for measuring arbitrarily shaped

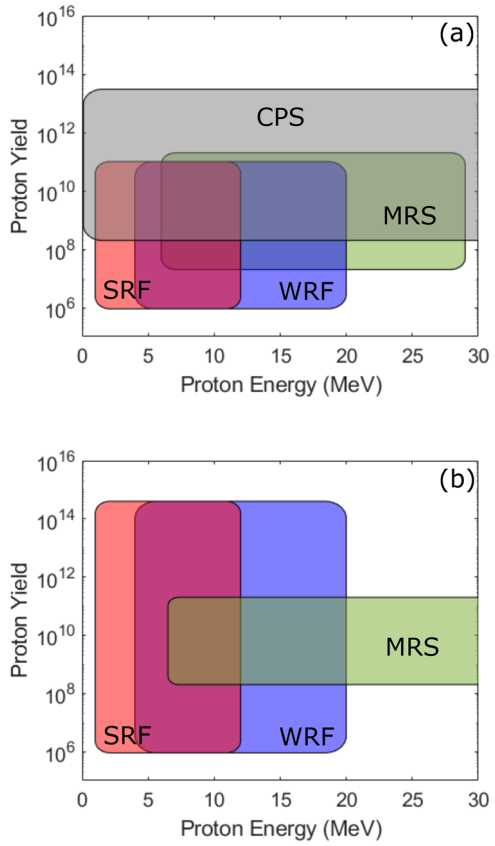

FIG. 1. Yield and energy coverage of a SRF, a wedge range filter (WRF), the OMEGA charged-particle spectrometers (CPSs), and the magnetic recoil spectrometer (MRS) on (a) OMEGA and (b) the NIF. Yield floors and ceilings are calculated assuming a maximum hit fluence of 7.4×10^2 and 7.4×10^5 counts/cm^2, respectively. In every case other than the NIF MRS, the yield range is achieved by using varying detector distances (SRF and WRF) or varying aperture sizes (CPS and MRS). On OMEGA, the SRFs are the only diagnostic that can measure energies below 4 MeV with yields below 2×10^8. On the NIF, the SRFs are the only diagnostic that can measure anything below 4 MeV. The upper energy limit shown for the SRF is determined by the designs that have been fielded to date. SRFs can, in general, be designed to have arbitrarily high upper energy limits.

charged-particle spectra with energies above roughly 1 MeV. When using this technique, SRFs are uniquely useful for measuring spectra that are continuous down to 0, such as the protons from ^{3}He^{3}He reactions,

$$^3\mathrm{He} + {}^3\mathrm{He} \rightarrow \alpha + \mathrm{p} + \mathrm{p}, \tag{2}$$

or the protons from T^{3}He reactions,

$$\mathrm{T} + {}^3\mathrm{He} \rightarrow \alpha + \mathrm{n} + \mathrm{p}, \tag{3}$$

whose lower energy behavior cannot be measured by other diagnostics. In the case of neutron-recoil spectrometers on the Z, this also allows for the measurement of down-scattered neutrons. Additionally, this technique can be applied to other charged-particles, such as deuterons from the T^{3}He reaction

$$\mathrm{T} + {}^3\mathrm{He} \rightarrow \alpha\,(4.8\,\mathrm{MeV}) + \mathrm{D}\,(9.5\,\mathrm{MeV}). \tag{4}$$

This paper is structured as follows: Section II discusses the new SRF designs and their capabilities as well as prescribes a basic procedure for designing SRFs for alternative applications. Section III discusses the new analysis method and highlights improvements over previous work. Section IV gives a detailed description of the SRF instrument response, and Sec. V describes a new more accurate calibration procedure. Finally, Sec. VI highlights examples of data obtained with the new SRF diagnostic.

II. DETECTOR DESIGN

Broadly speaking, an SRF is simply a CR-39 detector with some number of filters (> 1) in front of it. As such, the exact design of any single SRF can be highly customized with ease depending on the intended application. Additionally, an SRF can, in general, be applied to any CR-39 detector geometry, making it highly versatile. In this section, the basic procedure for designing an SRF will be discussed and a few designs will be presented toward the end. The remainder of this paper will largely focus on these designs, but it is important to note that all of the theory and capabilities discussed within can be generalized to alternative designs if needed.

An SRF can be loosely defined by its detector geometry, number of physical filters (N_f), and number of unique filter windows (N_w). A filter window is simply a spatial region on the CR-39 detector covered by one or more filters. Often, SRF filters are overlapped for fabrication purposes, meaning an individual window can have anywhere between 1 and all of the filters in front of it. An example of a SRF with $N_f = 7$ and $N_w = 7$ (a 7F7W SRF) can be seen in Figs. 2(a)–2(d) and a 5F9W SRF can be seen in Figs. 2(e)–2(h). Both of these designs use 5 cm diameter CR-39 detectors to be compatible with the geometry and mounting hardware of the existing Wedge Range Filter (WRF) spectrometers.[9,11] Ideally, an SRF will also have a background filter specifically designed to range out any potential signal. In the designs depicted in Fig. 2, this is accomplished by a 3 mm thick aluminum frame in the front of the stack of filters. This filter is important for background subtraction and does not count toward the > 1 filter requirement of an SRF.

Designing an SRF requires choosing appropriate window thicknesses for a given measurement. In general, the goal of a particular measurement can be defined by a particle type and detectable energy range $E \in [E^{\mathrm{SRF}}_{\mathrm{min}}, E^{\mathrm{SRF}}_{\mathrm{max}}]$. CR-39 detectors have 100% detection efficiency for some $E \in [E^{\mathrm{CR39}}_{\mathrm{min}}, E^{\mathrm{CR39}}_{\mathrm{max}}]$; the exact values vary[14] but are unimportant for the following discussion. Every filter arrangement in each window will downshift particles with some energy range $E_{\mathrm{in}} \in [E^{i}_{\mathrm{min}}, E^{i}_{\mathrm{max}}]$ such that energies of the particles when incident on the CR-39 are $E_{\mathrm{out}} \in [E^{\mathrm{CR39}}_{\mathrm{min}}, E^{\mathrm{CR39}}_{\mathrm{max}}]$. For example, if one were to consider protons and assume $E^{\mathrm{CR39}}_{\mathrm{min}} = 1$ MeV and $E^{\mathrm{CR39}}_{\mathrm{max}} = 3$ MeV, then 10 μm Ta would cause proton energies $E_{\mathrm{in}} \in [1.9, 3.6]$ MeV to be detectable on the CR-39. In practice, the exact values of $E^{\mathrm{CR39}}_{\mathrm{min}}$ and $E^{\mathrm{CR39}}_{\mathrm{max}}$ are dependent on processing details, analysis decisions, and even the intrinsic properties of an individual piece of CR-39. The values chosen here are reasonable estimations.

Choosing the thinnest and thickest filter arrangement for a window in an SRF is simply an exercise of setting $E^{\mathrm{thin}}_{\mathrm{min}} = E^{\mathrm{SRF}}_{\mathrm{min}}$ and $E^{\mathrm{thick}}_{\mathrm{max}} = E^{\mathrm{SRF}}_{\mathrm{max}}$. For example, if the goal was to cover all proton energies between 2 and 12 MeV, the thinnest and thickest window regions

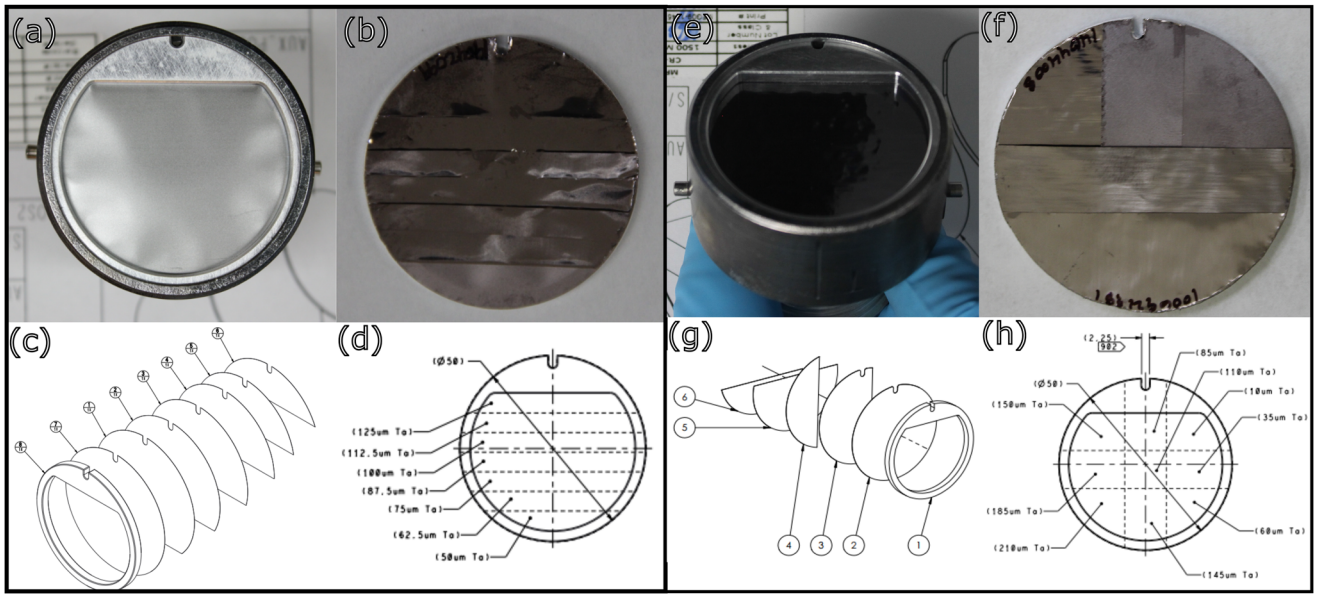

FIG. 2. Images and drawings of a couple SRF designs. (a)–(d) show a design with $N_f = 7$ and $N_w = 7$, while (e)–(h) show a design with $N_f = 5$ and $N_w = 9$. (a) and (e) show the SRFs as viewed from the source, and (b) and (f) show the SRFs as viewed from the CR-39. (c) and (g) show exploded view drawings, and (d) and (h) show individual filter windows as viewed from the source. All of the filters are made from tantalum, and the thick frame in front is 3 mm thick aluminum.

might be 10 and 240 μm of Ta, respectively. This is because for 10 μm Ta, detectable proton energies are $E_{\text{in}} \in [1.9, 3.6]$, while for 240 μm Ta, they are $E_{\text{in}} \in [11.3, 12.0]$. These numbers again assume $E_{\text{min}}^{\text{CR39}} = 1$ MeV and $E_{\text{max}}^{\text{CR39}} = 3$ MeV.

The only requirement for the remaining windows is that there exists some overlap in the energy coverage between subsequent windows. This requirement ensures that the analysis can search for self-consistency between window regions. To meet this requirement, we must choose some thickness t_{i+1} such that

$$E_{\text{min}}^{i+1} = E_{\text{min}}^{i} + f\left(E_{\text{max}}^{i} - E_{\text{min}}^{i}\right), \tag{5}$$

where t_{i+1} is the thickness of the next thickest filter after filter i and f is some fraction between 0 and 1.

TABLE I. 5F9W SRF designs for various particle measurements. Filter numbers correspond to the labels shown in Fig. 2(g). Each SRF uses a background filter frame (filter 1 in the figure) of 3 mm Al. All other filters are tantalum. Energy ranges are calculated using $E_{\text{min}}^{\text{CR39}} = 1.15$ (1.75) MeV and $E_{\text{max}}^{\text{CR39}} = 2.82$ (6.24) MeV for protons (deuterons). These energies come from typical track-diameter limits used in the SRF data analysis discussed in Sec. III.

Intended measurement	DD-p	T^3He-d	^{3}He^{3}He-p
Energy range (MeV)	[2.0, 5.5]	[5.9, 12.7]	[2.0, 11.1]
Filter 2 (μm)	10.0	50.0	10.0
Filter 3 (μm)	15.0	30.0	75.0
Filter 4 (μm)	15.0	30.0	75.0
Filter 5 (μm)	5.0	10.0	25.0
Filter 6 (μm)	5.0	10.0	25.0

Low values of f ensure more overlap, while high values reduce the number of required windows. Additional windows add robustness and flexibility to the fitting process. However, more windows will decrease the area and thus counts seen by any individual window. A general rule of thumb is to ensure that the number of counts in all windows exceeds 10^3, but this is rarely the limiting factor in practice. More practically, analysis, manufacturing, and calibration all get more complicated as N_f is increased, which often drives the desire to simplify.

Returning to the example of designing an SRF that can detect protons between 2 and 12 MeV, if we again assume $E_{\text{min}}^{\text{CR39}} = 1$ MeV and $E_{\text{max}}^{\text{CR39}} = 3$ MeV and take f to be 0.67, then Eq. (5) calculates that we should use a total of 15 windows with roughly 16.5 μm of Ta between each step. Again though, one may choose to use more or less windows depending on what is practical so long as some energy overlap exists between the windows.

The 5F9W SRF shown in Figs. 2(e)–2(h) innovates on the SRF formula by achieving nine unique filter regions with only five physical filters. This greatly simplifies both the manufacturing and calibration processes without sacrificing on the number of windows. Additionally, all of the designs fielded to date only require three unique filter thicknesses, which simplifies calibration even further since multiple filters can be taken from the same stock (thus having roughly the same thickness). Three different designs using the 5F9W geometry are summarized in Table I.

III. ANALYSIS THEORY

Previous work[12] established a forward-fit procedure to the track densities measured behind each window n_{meas}^{i}. In the previous analysis, one would assume that some spectrum S_{in} defined by some set of

parameters $\vec{p}$ was incident on the SRF. This spectrum is then down-ranged using Monte Carlo models, such as SRIM[15] or MCNP,[16] through each window to create a set of CR-39 incident spectra $\{S_{out}\}$. The expected track density in a given window is then given by

$$n^i_{model} = \frac{1}{4\pi\ell^2}\int_0^\infty dE_{out} S^i_{out}(E_{out},\vec{p})\eta_{\text{CR}-39}(E_{out}), \quad (6)$$

where ℓ is the CR-39's distance from the particle-source and $\eta_{\text{CR-39}}(E_{out})$ is the CR-39 detection efficiency to particles with energy E_{out}. The reduced chi-squared for the choice S_{in} is then

$$\chi^2_{red} = \frac{1}{N_w - N_{\vec{p}}}\sum_{i=1}^{N_w}\frac{\left(n^i_{model} - n^i_{meas}\right)^2}{\sigma^2_{n_i}}, \quad (7)$$

where N_w is the number of windows, $N_{\vec{p}}$ is the length of $\vec{p}$, and σ_{n_i} is the statistical uncertainty on the measurement n^i_{meas}.

One limitation of this method is its dependence on $\eta_{\text{CR-39}}(E_{out})$, which is not well understood and has been shown to vary between individual pieces of CR-39.[14] In practice, it is often approximated by the boxcar function

$$\eta_{\text{CR}-39}(E_{out}) \sim H(E_{out} - E_{\min}) - H(E_{out} - E_{\max}), \quad (8)$$

where H is the Heaviside step function and $E_{\min}$ and $E_{\max}$ are the minimum and maximum detection energies.

In reality, both $E_{\min}$ and $E_{\max}$ depend on how the CR-39 is processed and analyzed and on the intrinsic properties of the individual piece. This uncertainty was not previously considered in Ref. 12.

A new analysis technique inspired by the analysis of WRF data[9,11] has been developed to circumvent this problem. This technique relies on the energy–diameter relationship of the tracks in the CR-39. After taking data, every window region will have a large set of diameter tracks $\{D\}_i$. We circumvent the efficiency uncertainty by only considering diameters that correspond to particle energies guaranteed to satisfy $E \in [E_{\min}, E_{\max}]$. In practice, this means sub-selecting tracks with diameters that are sufficiently large. A general rule of thumb is to consider all tracks with diameters $D \in [0.5D_{\max}, 0.9D_{\max}]$, where $D_{\max}$ is the largest significant diameter.[14]

The analysis starts by assuming a particular relationship $f_{\text{DvE}}(E)$ that converts particle energies to track diameters uniquely. Suitable forms for this relationship are discussed in Ref. 14. Each window i then has its diameter sets converted into CR-39 incident energy sets $\{E_{out}\}_i$ using this relationship. These energies are then reverse-ranged using stopping-power tables to produce the set of SRF-incident energies $\{E_{in}\}_i$. When binned, these sets represent the inferred spectra that were incident on each individual window. Because, in practice, each window will see the same spectrum, all inferred window spectra should be consistent with one another in the spectral regions where they overlap. This criterion is ultimately what is used to test the validity of the initial choice of $f_{\text{DvE}}(E)$. A basic flow chart for this algorithm is shown in Fig. 3. Once a good choice for $f_{\text{DvE}}(E)$ is found, the final inferred spectrum is just the average of all of the window-inferred spectra. Visual demonstrations of this method are shown in Figs. 4 and 5.

Care needs to be taken with how self-consistency is determined between the window-inferred spectra. Having different filters means that each window sees different portions of the original spectrum.

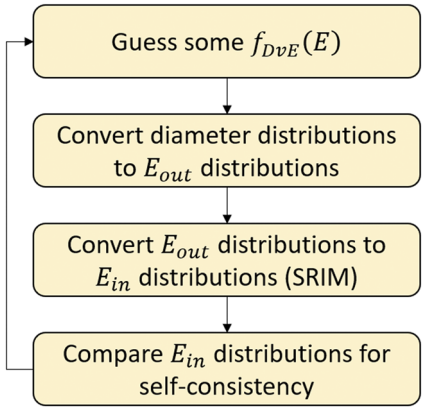

FIG. 3. Basic flow chart for the new SRF analysis technique. This process is looped through for all functions $\{f_{\text{DvE}}\}$ available for testing. The final spectrum is the average of the E_{in} distributions with strongest self-consistency (lowest χ^2).

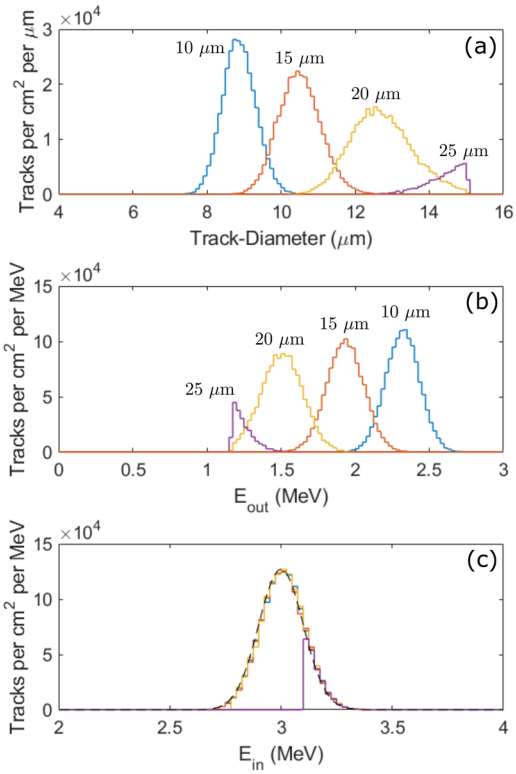

FIG. 4. Example of the analysis applied to simulated data. Approximately 10^9 protons were sampled from a Gaussian energy distribution with μ = 3.0 MeV and σ = 0.1 MeV. The spectrometer was a DD-p 5F9W SRF with filter thicknesses shown in Table I. The protons that landed on the CR-39 were converted to diameters and then back to energies by finding the best fit based on Eq. (9). (a) shows the diameter distributions behind each window, (b) shows inferred energy distributions behind each window, and (c) shows spectra as inferred by each window incident on the SRF. Thickness labels correspond to the total thickness seen by a given window. The black dashed curve in (c) is the original spectrum used to sample the particles.

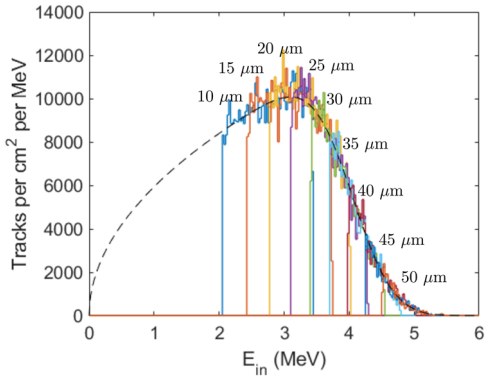

FIG. 5. Example of the analysis applied to simulated data. Approximately 10^9 protons were sampled from an energy distribution of the form $\sqrt{E}\left(1-\Phi\left(\frac{E-4.0\ \mathrm{MeV}}{0.5\ \mathrm{MeV}}\right)\right)$, where Φ is the cumulative distribution function of the standard normal distribution. This shape was constructed to resemble a wide non-peaked spectrum. The detector was a DD-p 5F9W SRF with filter thicknesses shown in Table I. The protons that landed on the CR-39 were converted to diameters and then back to energies by finding the best fit based on Eq. (9). Thickness labels correspond to the total thickness seen by each window. The black dashed curve is the original spectrum shape used to sample the particles.

This means each window-inferred spectrum will, in general, have different moments that cannot be directly compared. In general, sub-regions of spectral overlap need to be identified and compared. How this is done is somewhat arbitrary, but the following goodness parameter has been found to be effective,

$$\chi^2 = \frac{1}{N_E}\sum_j \frac{N_w(j)\sum_i\left(n_i^j\right)^2 - \left(\sum_i n_i^j\right)^2}{\left(\sum_i n_i^j\right)}, \tag{9}$$

where N_E is the number of energy bins with $N_w(j) > 1$, $N_w(j)$ is the number of filters that measure data between energy nodes E_j and E_{j+1}, and n_i^j is the density of counts between energy nodes E_j and E_{j+1} for window i. This χ^2 is a mean-normalized variance of count densities between each window averaged over every energy bin. It effectively compares the absolute magnitude of each energy node between all windows that happen to measure data there.

IV. DETECTOR RESPONSE

The detector response of any spectrometer is a crucial component of its performance. Detailed information about the shape of a spectrum can only be resolved if the response is well understood. For the SRFs, spectral broadening occurs via three main mechanisms: diameter blurring during the scanning process, artificial broadening in the analysis from poor filter-thickness calibration, and broadening due to energy straggling in the filters.

A. Diameter blurring

When the CR-39 is scanned by an optical microscope, variations in the diameters are observed. This diameter-blurring mechanism causes spectra inferred from diameter distributions to be wider than the original source. The exact cause of this diameter blurring is not well understood but is thought to be partially related to

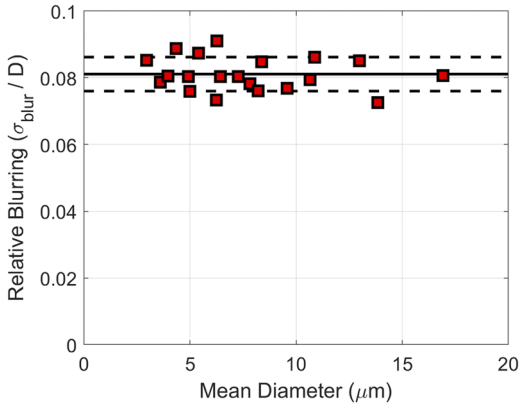

FIG. 6. Relative diameter blurring observed from the experiment depicted in Fig. 20. Red data points are observed values from a single CR-39 piece etched for 2, 3, 4, 5, and 6 h. The black solid line is the mean value, and the black dashed lines represent $\pm 1\sigma$ from the mean. The effects of relative diameter blurring are invariant to the mean diameter or etch time, averaging out to 8.1 ± 0.5%.

varying focusing during the scan. The magnitude of this effect was determined from an experiment described in the Appendix and is summarized in Fig. 6 for various etch times and mean diameters.

As seen in Fig. 6, relative diameter broadening is invariant to etch time and mean diameter, staying constant at $\sigma_{\mathrm{blur}}/D = 8.1 \pm 0.5\%$. How this translates to spectral broadening is somewhat complicated due to the fact that many diameters are used in the analysis and by the fact that the relation between track-diameters and particle energy varies from CR-39 to CR-39.[14] A simulated example of the fully integrated effect is shown in Fig. 7. To demonstrate how this effect varies with f_{DvE}, a full mapping of

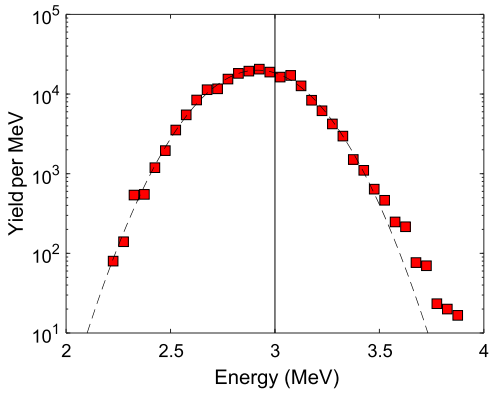

FIG. 7. Simulated SRF inferred spectrum from a mono-energetic 3.0 MeV proton source subjected to a diameter blurring of $\sigma_{\mathrm{blur}}/D = 8.1\%$. The effects of energy straggling were not modeled to isolate the effect of diameter-blurring. Simulated data are shown as red squares, while the black dashed curve is a Gaussian fit to the data. Energy straggling in the filters is not considered in the simulations. Diameter to energy mapping was modeled using the c-Parameter model described in Ref. 14. A c-parameter of 1.0 was used in the mapping, and a c-Parameter of 1.05 was inferred in the analysis of the broadened distributions. The resulting mean energy and FWHM of the fit were 2.92 MeV and 493 keV, respectively. The resulting spectrum is not perfectly Gaussian, having a notable high energy tail due to the non-linear relation between track-diameters and particle energies.

the broadening with different diameter–energy relations is shown in Fig. 8.

B. Broadening due to filter thickness uncertainty

If the SRF filter thicknesses are not properly calibrated, additional artificial broadening can be induced in the analysis. This occurs when the individual window spectrum cannot be made to agree due to the discrepancy between the real thicknesses and the assumed thicknesses. An example of this on simulated data is shown in Fig. 9.

An additional side-effect of poor filter thickness calibration is how it interacts with the analysis procedure discussed in Sec. III. The analysis attempts to compensate for poor filter thickness values by finding an $f_{\mathrm{DvE}}(E)$ that can best match window spectra to one another. This choice of $f_{\mathrm{DvE}}(E)$ will, in general, not match the true best function derived from using the correct filter thickness

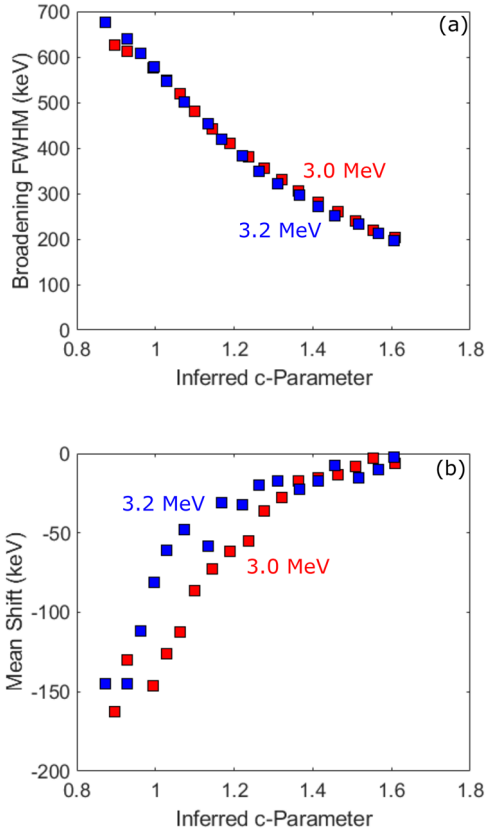

FIG. 8. Simulated mapping between broadening and mean energy shifts caused by diameter blurring for different diameter–energy relationships. The diameter–energy relationship is defined by a single c-Parameter described in Ref. 14. (a) shows the impact of the c-Parameter on broadening while (b) shows the impact on the mean energy. Lower c-Parameters generally have softer slopes in f_{DvE} (lower absolute values of $\frac{dD}{dE}$). These results therefore imply that particles with softer diameter–energy relation slopes are broadened more severely. Red (blue) data were generated by simulating a mono-energetic 3.0 (3.2) MeV proton source onto an SRF and subjecting the resultant diameters to a blurring of $\sigma_{\mathrm{blur}}/D = 8.1\%$.

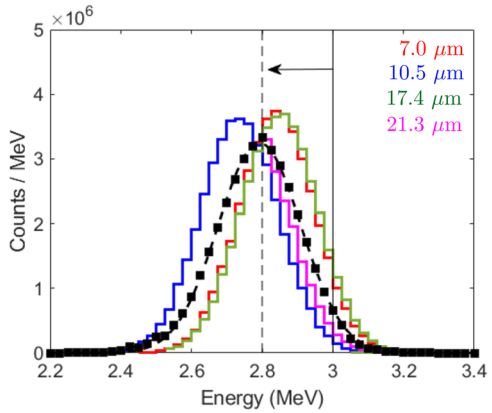

FIG. 9. Simulated broadening caused by poor filter-thickness calibration. The input spectrum was a proton source normally distributed with $\mu = 3.0$ MeV and $\sigma = 100$ keV. The actual windows were Ta with nominal densities of 16.65 g/cm^3 and thicknesses of 10, 15, 20, and 25 μm. The data were analyzed assuming incorrect window thicknesses of 7.0, 10.5, 17.4, and 21.3 μm. Each window generates its own spectrum shown in the figure as red, blue, green, and magenta curves. The black data points are the average of the window spectra (and thus the final inferred spectrum), and the black dashed curve is the best fit to the average. The fit to the average spectrum inferred $\mu = 2.78$ MeV and $\sigma = 120$ keV.

values. This itself also impacts the width of the inferred spectra by changing the slope of the diameter–energy relationship characterized by the c-parameter discussed in Ref. 14. In some cases, this can actually narrow the inferred spectra. The exact effect is sensitive to the differential between the assumed thicknesses and the true thicknesses and thus is difficult to capture. To test this, several simulated DD-p 5F9W SRFs were exposed to a normally distributed proton source with $\mu = 3.0$ MeV and $\sigma = 100$ keV. The filter thicknesses of each SRF were randomly perturbed about their true values with a relative σ of 15% and then analyzed using the nominal values. The inferred mean energies and spectral widths were then tallied, the results of which are summarized in Fig. 10.

As can be seen in Fig. 10, random perturbations on the filter thicknesses shift the inferred mean energy symmetrically about the true value. The inferred widths, however, are generally wider than the true value. This shift in the distribution is the broadening due to poor filter-thickness calibration. We note again that a non-negligible portion of the distribution actually has narrower inferred widths. The exact values for the distributions shown in Fig. 10 are also sensitive to the original source spectrum and SRF design. As a result, we recommend that this exercise be repeated per application/SRF design to determine how accurately the filter thicknesses need to be known.

Finally, we note that the analyzer has full access to the spectra inferred for each individual window, making it possible to determine when this broadening mechanism is occurring. This, perhaps, opens the door to *in situ* filter calibrations whenever it becomes clear that the filters are not properly calibrated. In general, this cannot be a sufficient replacement to true calibrations. This is well illustrated by the example given in Fig. 9. Here, all four of the window spectra fall short of the true mean value of 3.0 MeV due to all of the assumed filter thicknesses being too thin. While it is clear that the filters are poorly calibrated relative to each other, there is no signature in the

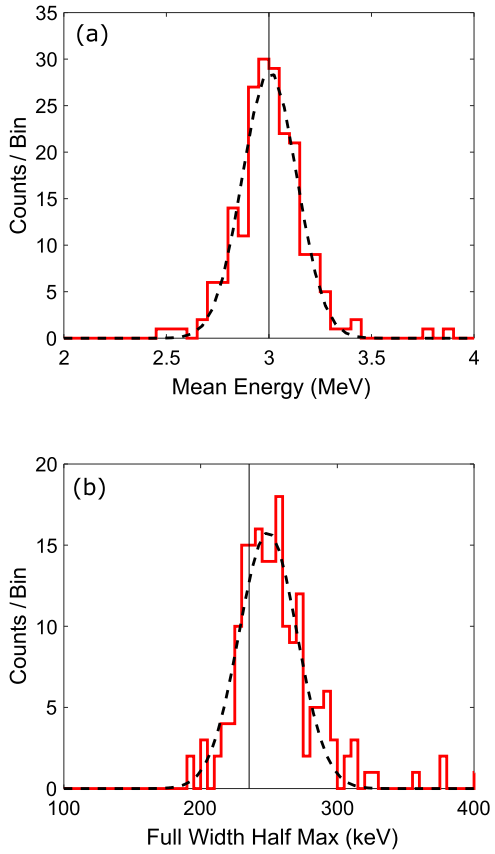

FIG. 10. Distributions of inferred quantities from simulated SRFs with perturbed filter thicknesses. The source spectrum for all simulations was a normally distributed proton source with μ = 3.0 MeV and σ = 100 keV. Filter thicknesses were randomly perturbed about their true value with a relative σ of 15%. (a) shows the distribution of inferred mean energies, and (b) shows the distribution of the inferred widths. The red lines are histograms of the data, the black dashed curves are fits to the data, and the black vertical solid lines are the true values of the source spectrum. For this example, the corresponding uncertainties in mean energy and spectral width are 8.8 and 1.4 keV/% uncertainty in filter thicknesses, respectively.

data to illuminate where the true mean value should lie. Still, altering the filter thicknesses to get better agreement would give a better estimate of the spectral width. That said, we note again that changes in $f_{\mathrm{DvE}}(E)$ also alter the widths of the window spectra. For these reasons, we simply recognize that *in situ* calibrations have a promising potential but are subject to details that go beyond the scope of this paper.

C. Filter energy straggling

Additional broadening can occur simply due to energy straggling in the SRF filters. Energy straggling is the broadening in particle energies due to statistical variations in small-angle collisions throughout the filter medium. As a result, mono-energetic particles incident onto an SRF will have non-mono-energetic distributions once they are incident on the CR-39 detector.

To investigate this broadening, an SRF was modeled with MCNP6.[16] The SRF was exposed to several mono-energetic proton and deuteron lines of varying energies and the resultant CR-39 incident spectra behind each window were recorded. These spectra were converted to diameter distributions using the c-Parameter model discussed in Ref. 14. These diameter distributions were analyzed using the technique established in Sec. III. The widths of the resultant spectra reflect the broadening caused by straggling. The results of this exercise are shown in Fig. 11.

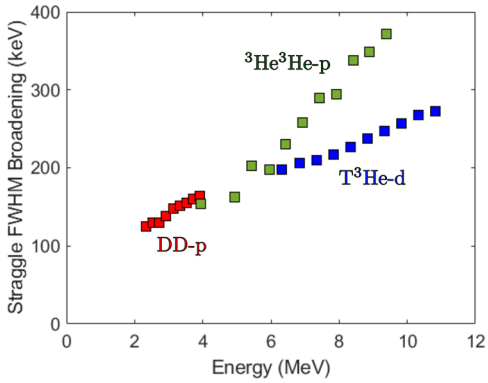

FIG. 11. Broadening due to energy straggling in the SRF filters. Data were simulated in MCNP6 by exposing an SRF to mono-energetic sources and converting the resulting CR-39 incident energy distributions into diameter distributions. Energy to diameter mapping was done using the c-Parameter model discussed in Ref. 14 with a c-Parameter of 1.30. The diameter distributions were then analyzed using the technique discussed in Sec. III and the resulting spectral width is shown here. Data in red, blue, and green correspond to the 5F9W DD-p, T^3He-d, and ^{3}He^{3}He-p SRF designs shown in Table I, respectively. The blue data were generated using deuterons, and the others were generated with protons.

As can be seen in Fig. 11, the broadening due to energy straggling is generally low when compared to the diameter blurring mechanism shown in Fig. 8(a). It is, however, more significant than the filter uncertainty mechanism shown in Fig. 10(b). In general, diameter blurring is the dominant broadening mechanism of the three.

V. DETECTOR CALIBRATION

The spectral accuracy of the SRF is partially dictated by the accuracy to which the areal density (ρL) of each individual filter is known. Generally, filter thicknesses of order 10 μm are used, which can be difficult to accurately characterize. Often, manufacturers provide thicknesses within 10%–15% tolerances, which can result in large energy uncertainties, as shown in Fig. 10.

Micrometer measurements are often used to reduce this uncertainty, but even this method is limited. Micrometers provide no information about the density (ρ) of the material in question, so one often has to assume it. Additionally, micrometers can often give inconsistent results when working with thinner materials. Regardless, this method is still valuable when finer characterizing techniques are unavailable.

One technique for calibrating the SRFs is through fully integrated spectral measurements. The basic methodology for this technique is to measure well known spectra with a fully assembled SRF. If a single SRF with N_f filters measures N_f unique spectra, then the filter areal densities should, in principle, be uniquely quantified. It

should be specifically noted that N_f, not N_w, is what dictates the required number of measurements. This fact motivates designing SRFs with filter overlaying to maximize N_w for the measurement accuracy while minimizing N_f for calibration simplicity.

Recently, this technique was applied to the DD-p 5F9W SRF design described in Table I using the MIT-HEDP Accelerator Facility.[17] Four unique DD-proton spectra were generated by using varying laboratory angles and external filters. While the design has five total filters, only four of them measured these spectra and thus were calibrated. A cartoon of the exact calibration setup is shown in Fig. 12, and the resultant spectra are shown in Fig. 13. Additionally, sample calibration results are shown in Fig. 14.

After the data are obtained, the calibration is simply a process of finding the set of areal densities that minimize the function

$$\epsilon = \sqrt{\epsilon_E^2 + \epsilon_\sigma^2}, \tag{10}$$

where ϵ_E is the error in the mean energy given by

$$\epsilon_E^2 = \sum_i \left(\frac{E^i_{SRF} - \left[E^i + \delta^i_E(f_{\mathrm{DvE}})\right]}{E^i + \delta^i_E(f_{\mathrm{DvE}})} \right)^2, \tag{11}$$

where E^i_{SRF} is the mean energy of the ith source as determined by the SRF, E^i is the true source mean energy, and δ^i_E is the energy shift caused by diameter broadening. ϵ_σ is the error in the spectral width

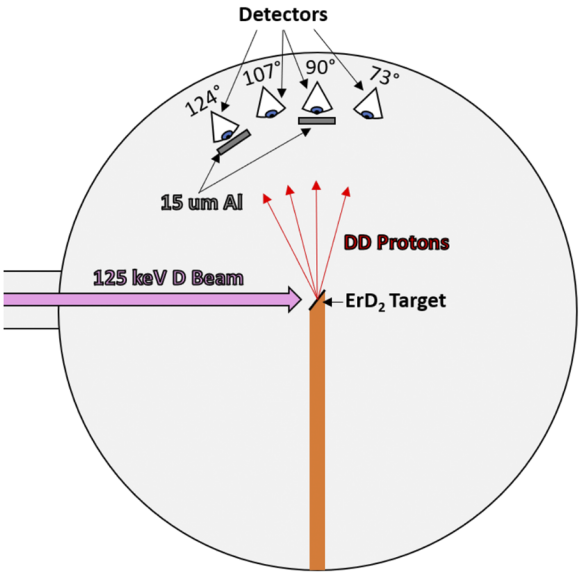

FIG. 12. Cartoon of the experimental setup used to calibrate the SRF design depicted in Figs. 2(e)–2(h). A 125 kV beam of deuterons is accelerated into an ErD_2 target, which results in DD fusion protons. The protons are measured from laboratory angles of 73°, 90°, 107°, and 124° to get spectra with different mean energies. Measurements at 90° and 124° were filtered with 15 μm of aluminum to further exacerbate the energy difference between spectra. All spectra were measured using a single Silicon Surface Barrier Detector (SBD). Each individual SRF measured all four spectra and were calibrated such that they agreed with the SBD measurement.

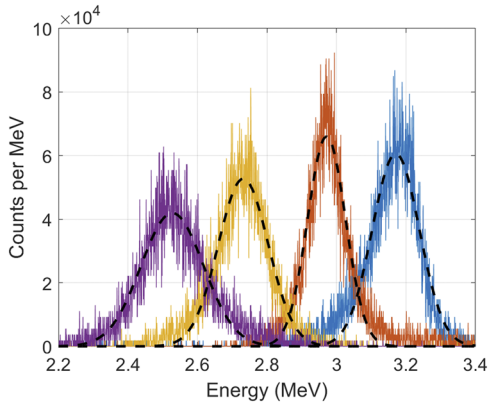

FIG. 13. Four spectra measured using a fully depleted AMETEK Silicon Surface Barrier Detector (SBD). The spectra came from the four detector positions/configurations depicted in Fig. 12. The blue, orange, yellow, and purple data correspond to laboratory angles of 73°, 107°, 90°, and 124°, respectively. The 90° and 124° measurements were filtered by 15 μm of aluminum.

and is similarly given by

$$\epsilon_\sigma^2 = \sum_i \left(\frac{\sigma^i_{SRF} - \sqrt{(\sigma^i)^2 + (\delta^i_\sigma(f_{\mathrm{DvE}}))^2}}{\sqrt{(\sigma^i)^2 + (\delta^i_\sigma(f_{\mathrm{DvE}}))^2}} \right)^2, \tag{12}$$

where σ^i_{SRF} is the standard deviation of the ith source as determined by the SRF, σ^i is the true source standard deviation, and δ^i_σ is the combined broadening caused by the diameter broadening and energy straggling. Note that in our case, $\delta^i_\sigma > \sigma^i$ and Eq. (12) approximately reduces to a comparison of the expected broadening and not of the actual source width. Despite that, Eq. (12) is still a valuable constraint due to the filter uncertainty broadening mechanism discussed in Sec. IV. It should be noted that the weighting of Eq. (10)

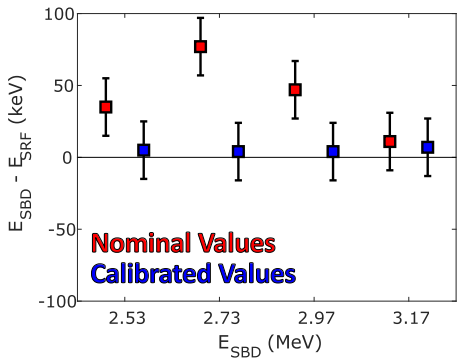

FIG. 14. Example results of the calibration of an SRF using the experimental setup depicted in Fig. 12. The SRF data shown were gathered from accelerator shots A2019121202-05. The red data points show the SRF error when using nominal Ta areal density values of 16.65, 8.325, 8.325, and 24.975 mg/cm^2. The blue data points show the error when using calibrated Ta areal densities of 19.66, 7.08, 8.64, 22.90 mg/cm^2. Prior to calibration, the SRF agreed with the SBD within an 80 keV uncertainty. Once calibrated, the SRF agrees with the SBD values within a 20 keV uncertainty. The SBD has a systematic uncertainty of 20 keV, resulting in a final systematic uncertainty of 30 keV for this SRF.

has no theoretical basis and is just an *ad hoc* function that was found to give good calibration results shown in Fig. 15.

This is essentially an optimization problem with N_f free parameters. The dimensionality of this problem can become problematic as N_f gets too large. In such cases, Monte Carlo approaches are recommended to decrease computational requirements.

It is important to note that the minimization of Eq. (11) or Eq. (12) is not sufficient for calibration. There are degenerates in the areal density parameter space that allow matching the mean energies or the spectral widths with areal densities far away from the true values. This is well demonstrated in Fig. 15. Here, simulated data were generated using known filter areal densities and then several random filter configurations were used to analyze the data in an attempt to re-derive the correct configuration. As can be seen, minimization of ϵ_E and ϵ_σ alone was not sufficient to derive the correct configuration. The combined error (ϵ) was necessary.

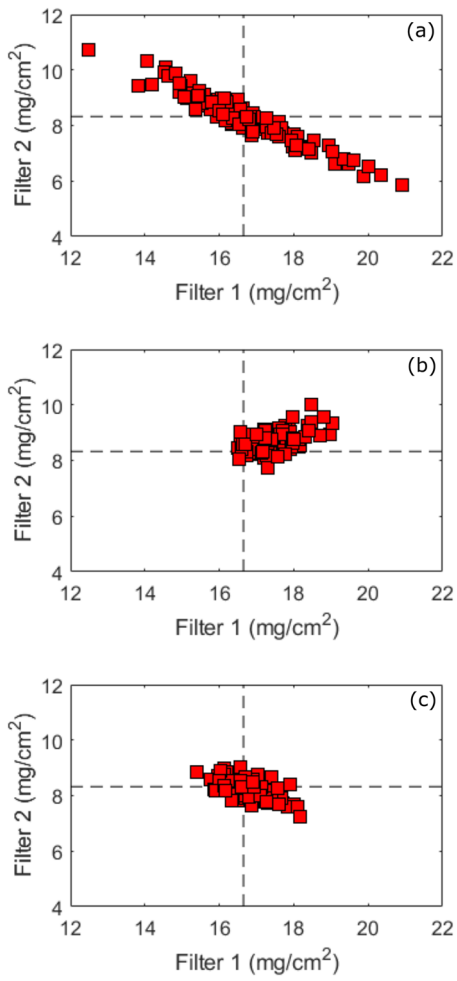

FIG. 15. Sub-selections of 6400 randomly generated SRF filter configurations used to analyze simulated data. (a)–(c) are the 100 solutions with minimum ϵ_E, ϵ_σ, and ϵ, respectively. The black dashed lines represent the areal density values used to simulate the data being analyzed. Minimization of ϵ_E results in a large degeneracy, and minimization of ϵ_σ is not sufficient to converge to the proper solution. Minimization of ϵ properly converges about the true calibration values.

VI. EXPERIMENTAL RESULTS

In this section, we present and discuss various experimental examples of SRF data that has been analyzed with the technique discussed in Sec. III.

First, we start with an example of data taken from the MIT-HEDP Accelerator Facility.[17] A 5F9W SRF measured DD protons ranged through 15 μm of aluminum. This spectrum was also measured using an AMETEK SBD for comparison. The results of this experiment are shown in Fig. 16.

As can be seen in Fig. 16, the SRF does an excellent job of matching the mean energy inferred by the SBD. On the other hand, the SRF spectrum is wider than the SBD spectrum due to the various broadening mechanisms discussed in Sec. IV. Here, the total broadening is roughly 230 keV, which is of the order of (albeit noticeably lower than) the results plotted in Fig. 8.

Next, we show an example of data taken from the OMEGA laser facility (Fig. 17). This figure shows a DD-proton spectrum emitted from an implosion measured by both a DD-p 5F9W SRF and CPS2. SRF and CPS2 are in good agreement on the absolute yield and the mean energy. Again, we see that the SRF spectrum is broader than the CPS spectrum corresponding to a minimum instrumental SRF broadening of 357 keV. Again, this is of the order expected from Fig. 8, but in this case, it is a bit larger.

Next is a demonstration of a 7F7W SRF being used to measure T^3He deuterons generated from an implosion experiment performed on the NIF. In this example, the deuterons were measured by several SRFs and MRS. Figure 18 shows these data as inferred by the two diagnostics.

In Fig. 18, we see that both diagnostics capture the general shape of the spectrum, a Gaussian with a low energy tail due to the

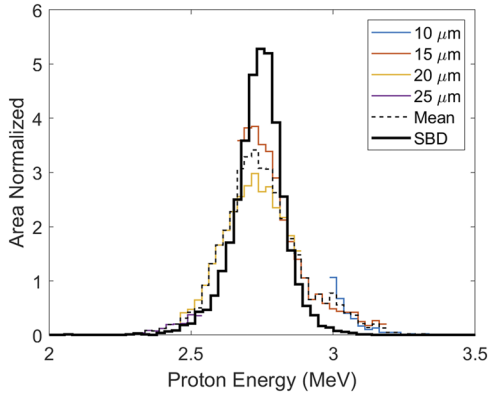

FIG. 16. SRF and SBD measured spectra from a DD-proton source ranged through 15 μm of aluminum at the MIT-HEDP Accelerator Facility shot number A2020021001. The black solid histogram and the black dashed histogram represent the spectrum as inferred by the SBD and SRF, respectively. For comparison, the colored histograms represent the spectrum as inferred by the individual Ta filters of the SRF with their thicknesses labeled in the legend. The mean energies of the SRF and SBD spectra are 2.72 and 2.73 MeV, respectively. The FWHM of the SRF and SBD are 277 and 170 keV, respectively. This corresponds to an SRF instrument broadening of 230 keV. The SRF spectrum was inferred with a c-Parameter of 1.21.

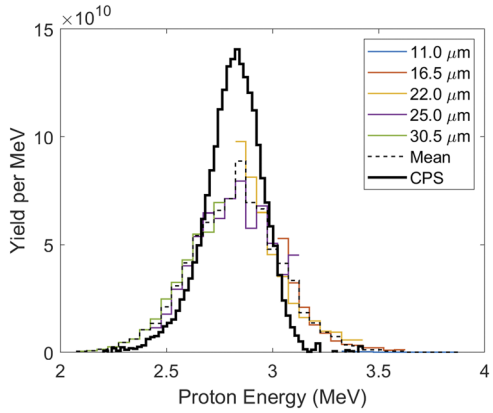

FIG. 17. SRF and CPS2 measured spectra from a DD-proton source generated on OMEGA shot number 96209. The black solid and the black dashed histogram represent the spectrum as inferred by CPS2 and SRF, respectively. For comparison, the colored histograms represent the spectrum as inferred by the individual Ta filters of the SRF with their thicknesses labeled in the legend. The yields of the SRF and CPS2 spectra are 4.0×10^{12} and 4.2×10^{12}, respectively. The mean energies of the SRF and CPS2 spectra are 2.79 and 2.82 MeV, respectively. The FWHM of the SRF and CPS2 is 465 and 298 keV, respectively. This corresponds to an SRF instrument broadening of 357 keV. The SRF spectrum was inferred with a c-Parameter of 1.45.

areal density evolution of the implosion. The SRF-measured spectrum has an artificial high energy tail because it also measured a T^3He proton continuum that sits beneath the deuteron signal. The MRS is not subject to this issue due to its magnetic system separating the two signals. The mean energies are in good agreement, with differences thought to be due to asymmetries along the spectrometers' lines of sight. Once again, the SRF signal is broadened relative to

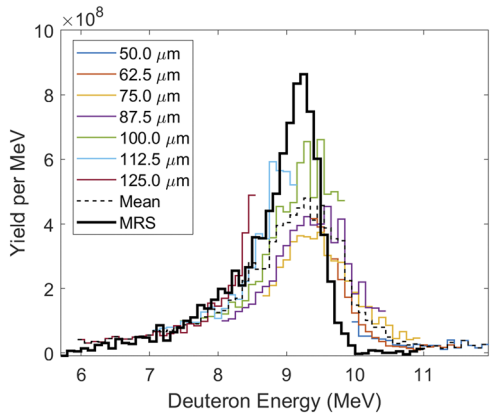

FIG. 18. SRF and MRS-measured spectra from a T^3He deuteron source generated on NIF shot number N161214-001-999. The black solid and the black dashed histogram represent the spectrum as inferred by MRS and SRF, respectively. For comparison, the colored histograms represent the spectrum as inferred by the individual Ta filters of the SRF with their thicknesses labeled in the legend. The yields of the SRF and MRS spectra are 8.5×10^8 and 9.2×10^8, respectively. The mean energies of the SRF and MRS spectra are 9.24 and 9.17 MeV, respectively. The FWHM of the SRF and MRS spectra is 1.04 and 0.61 MeV, respectively. This corresponds to an SRF instrument broadening of 839 keV. The SRF spectrum was inferred with a c-Parameter of 0.8.

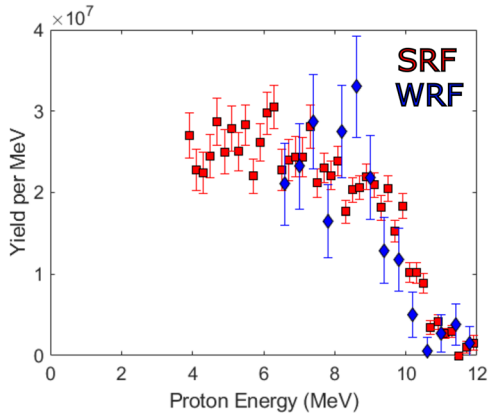

FIG. 19. Preliminary SRF and WRF measured $^3He^3He$ proton spectra from NIF shot N200211-002-999. The red squares show the spectrum as inferred by the SRF, and the blue diamonds show the spectrum as inferred by a WRF.

the MRS signal. Here, the broadening must be at least 839 keV. This large broadening is expected for deuterons due to the low c-Parameter required to describe the diameter–energy relationship. Additional broadening is thought to come from the T^3He proton background.

Finally, Fig. 19 shows an example of $^3He^3He$ protons from an implosion experiment on the NIF being measured by a WRF and a 5F9W SRF. This example well demonstrates the newly developed analysis's ability to recover arbitrary spectral shapes. As can be seen in the figure, the SRF and WRF are in good agreement.

VII. CONCLUSIONS

In this paper, we have greatly expanded the capabilities of the SRF spectrometer. A new 5F9W SRF design was developed with three configurations for measuring common charged-particle spectra at the NIF and OMEGA. Additionally, a procedure for designing custom SRFs was established.

A new analysis technique for measuring arbitrary spectra was developed. This technique is extremely versatile and allows for measurement of higher order features not previously possible with the SRF spectrometers. This includes continuous non-peaked spectra (such as $^3He^3He$-p spectra) as well as spectra with skews and long down-scatter features. This capability is not only advantageous for charged-particle measurements but is also crucial for the measurement of down-scattered neutrons in a proposed Z neutron-recoil spectrometer.[5]

This work has extensively explored the response of the SRF spectrometers. Three different broadening mechanisms were identified: diameter blurring, filter thickness uncertainties, and filter energy straggling with diameter blurring generally being the dominant mechanism.

A new calibration technique for the SRFs has been developed and demonstrated in this work. This calibration procedure allows for more precise mean energy measurements than previously possible.

Finally, these improvements and new capabilities were all demonstrated on real experimental data from the NIF and OMEGA. This provides additional confidence in all of these developments.

ACKNOWLEDGMENTS

The authors sincerely thank the OMEGA and NIF operations staff who supported this work and Bob Frankel, Ernie Doeg, and Michelle Valadez for processing the CR-39. This material is based upon work supported by the Department of Energy, National Nuclear Security Administration under Center of Excellence Award No. DE-NA0003868, the National Laser Users' Facility under Award No. DE-NA0003539, and LLE under Award No. 417532-G. This report was prepared as an account of work sponsored by an agency of the United States Government. Neither the United States Government nor any agency thereof, nor any of their employees, makes any warranty, express or implied, or assumes any legal liability or responsibility for the accuracy, completeness, or usefulness of any information, apparatus, product, or process disclosed, or represents that its use would not infringe privately owned rights. Reference herein to any specific commercial product, process, or service by trade name, trademark, manufacturer, or otherwise does not necessarily constitute or imply its endorsement, recommendation, or favoring by the United States Government or any agency thereof. The views and opinions of authors expressed herein do not necessarily state or reflect those of the United States Government or any agency thereof.

APPENDIX: DIAMETER BLURRING EXPERIMENT

To quantify the effect of diameter blurring, a single SRF was exposed to 3 MeV DD protons at the MIT-HEDP Accelerator Facility. This SRF had $N_w = 4$ windows with aluminum filters of areal densities of 56.7, 110.7, 151.2, and 178.2 mg/cm^2. Prior to the experiment, each filter was calibrated individually using a SBD for the measurement of the energy downshifts. A cartoon of the experimental setup is shown in Fig. 20. The resulting SBD spectra and SRF diameter distributions for each of the filters are shown in Fig. 21.

With the data shown in Fig. 21, it is possible to come up with relationships between the track diameters and particle energies using models described in Ref. 14. With these fits established, one can calculate how much broadening to expect in the diameter distributions from sources other than diameter blurring. The sources include the finite width of the fusion source [full-width-half-maximum (FWHM) of 130 keV] and energy straggling in the filters. The effects of straggling were determined using TRIM[15] and are shown in Table II. The contribution of diameter blurring is then

$$\frac{\sigma_{\text{blur}}}{D} = \frac{1}{D}\sqrt{\sigma^2_{\text{meas}} - \sigma^2_{\text{other}}}, \tag{A1}$$

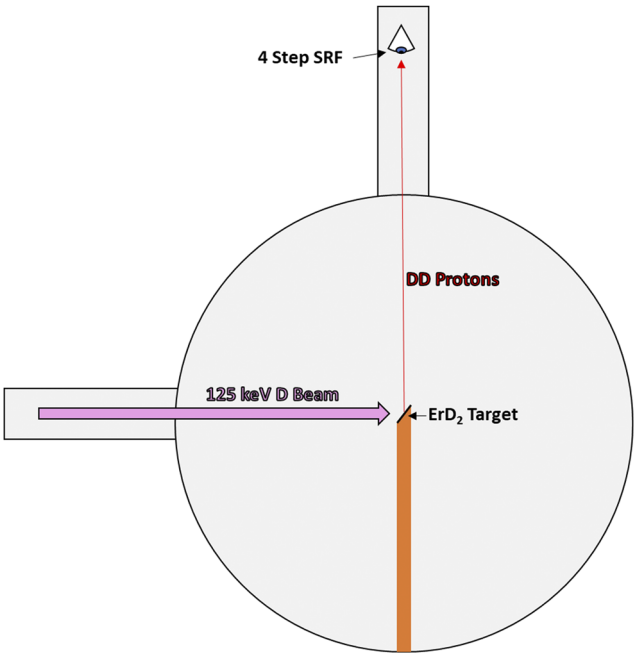

FIG. 20. Cartoon of the experimental setup used to investigate the effects of diameter blurring. A 125 kV beam of deuterons is accelerated onto an ErD_2 target, which results in DD fusion protons. A single four step SRF was fielded approximately at 90° relative to the beam and 60 cm away from the ErD_2 target to minimize the solid angle sampled by the spectrometer.

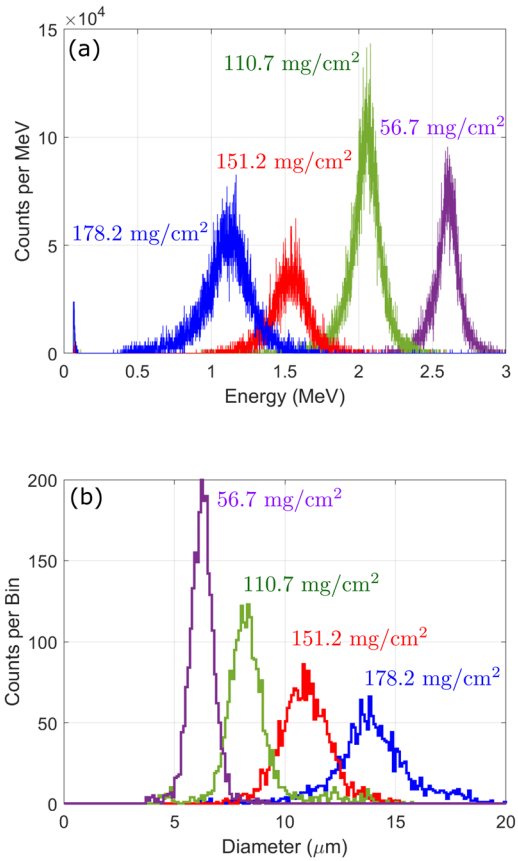

FIG. 21. Data gathered from an experiment to quantify the effects of diameter blurring. (a) shows the spectral data measured by an AMETEK SBD for four aluminum filters, and (b) shows the diameter distributions measured on CR-39 using the exact same filters. The distributions in purple, green, red, and blue correspond to aluminum filters with areal densities of 56.7, 110.7, 151.2, and 178.2 mg/cm^2, respectively. The order of the peaks swaps between (a) and (b) because particle energy and track diameter are inversely related. The data shown in (b) correspond to an etch time of 5 h.

TABLE II. The spectral broadening effects of straggling through aluminum filters as determined by TRIM. The values in the second column were determined by modeling a 3 MeV proton source going through the appropriate amount of aluminum. Values in the third column are the final effective width of a proton source with a FWHM of 130 keV prior to entering the filter.

Filter ρL (mg/cm^2)	TRIM FWHM (keV)	Final FWHM (keV)
56.7	52.6	140.2
110.7	82.2	153.8
151.2	110.2	170.4
178.2	141.0	191.8

where σ_{meas} is the standard deviation of the diameter distribution, σ_{other} is the calculated standard deviation from the finite fusion source width and energy straggling, and D is the mean diameter of the distribution. The results of this calculation for all filters and various etch times are shown in Fig. 6.

DATA AVAILABILITY

The data that support the findings of this study are available from the corresponding author upon reasonable request.

REFERENCES

[1]G. H. Miller, E. I. Moses, and C. R. Wuest, Nucl. Fusion **44**, S228 (2004).

[2]T. R. Boehly, D. L. Brown, R. S. Craxton, R. L. Keck, J. P. Knauer, J. H. Kelly, T. J. Kessler, S. A. Kumpan, S. J. Loucks, S. A. Letzring, F. J. Marshall, R. L. McCrory, S. F. B. Morse, W. Seka, J. M. Soures, and C. P. Verdon, Opt. Commun. **133**, 495 (1997).

[3]D. T. Casey, J. A. Frenje, M. G. Johnson, F. H. Séguin, C. K. Li, R. D. Petrasso, V. Y. Glebov, J. Katz, J. Magoon, D. D. Meyerhofer, T. C. Sangster, M. Shoup, J. Ulreich, R. C. Ashabranner, R. M. Bionta, A. C. Carpenter, B. Felker, H. Y. Khater, S. LePape, A. MacKinnon, M. A. McKernan, M. Moran, J. R. Rygg, M. F. Yeoman, R. Zacharias, R. J. Leeper, K. Fletcher, M. Farrell, D. Jasion, J. Kilkenny, and R. Paguio, Rev. Sci. Instrum. **84**, 043506 (2013).

[4]J. A. Frenje, T. J. Hilsabeck, C. W. Wink, P. Bell, R. Bionta, C. Cerjan, M. G. Johnson, J. D. Kilkenny, C. K. Li, F. H. Séguin, and R. D. Petrasso, Rev. Sci. Instrum. **87**, 11D806 (2016).

[5]B. Lahmann, M. G. Johnson, K. D. Hahn, J. A. Frenje, D. J. Ampleford, B. Jones, M. A. Mangan, A. Maurer, C. L. Ruiz, F. H. Séguin, and R. D. Petrasso, Rev. Sci. Instrum. **91**, 073501 (2020).

[6]M. E. Cuneo, M. C. Herrmann, D. B. Sinars, S. A. Slutz, W. A. Stygar, R. A. Vesey, A. B. Sefkow, G. A. Rochau, G. A. Chandler, J. E. Bailey, J. L. Porter, R. D. McBride, D. C. Rovang, M. G. Mazarakis, E. P. Yu, D. C. Lamppa, K. J. Peterson, C. Nakhleh, S. B. Hansen, A. J. Lopez, M. E. Savage, C. A. Jennings, M. R. Martin, R. W. Lemke, B. W. Atherton, I. C. Smith, P. K. Rambo, M. Jones, M. R. Lopez, P. J. Christenson, M. A. Sweeney, B. Jones, L. A. McPherson, E. Harding, M. R. Gomez, P. F. Knapp, T. J. Awe, R. J. Leeper, C. L. Ruiz, G. W. Cooper, K. D. Hahn, J. McKenney, A. C. Owen, G. R. McKee, G. T. Leifeste, D. J. Ampleford, E. M. Waisman, A. Harvey-Thompson, R. J. Kaye, M. H. Hess, S. E. Rosenthal, and M. K. Matzen, IEEE Trans. Plasma Sci. **40**, 3222 (2012).

[7]D. G. Hicks, C. K. Li, R. D. Petrasso, F. H. Séguin, B. E. Burke, J. P. Knauer, S. Cremer, R. L. Kremens, M. D. Cable, and T. W. Phillips, Rev. Sci. Instrum. **68**, 589 (1997).

[8]D. G. Hicks, "Charged-particle spectroscopy: A new window on inertial confinement fusion," Ph.D. thesis, Massachusetts Institute of Technology, 1999.

[9]F. H. Séguin, J. A. Frenje, C. K. Li, D. G. Hicks, S. Kurebayashi, J. R. Rygg, B.-E. Schwartz, R. D. Petrasso, S. Roberts, J. M. Soures, D. D. Meyerhofer, T. C. Sangster, J. P. Knauer, C. Sorce, V. Y. Glebov, C. Stoeckl, T. W. Phillips, R. J. Leeper, K. Fletcher, and S. Padalino, Rev. Sci. Instrum. **74**, 975 (2003).

[10]A. B. Zylstra, J. A. Frenje, F. H. Séguin, M. J. Rosenberg, H. G. Rinderknecht, M. G. Johnson, D. T. Casey, N. Sinenian, M. J.-E. Manuel, C. J. Waugh, H. W. Sio, C. K. Li, R. D. Petrasso, S. Friedrich, K. Knittel, R. Bionta, M. McKernan, D. Callahan, G. W. Collins, E. Dewald, T. Döppner, M. J. Edwards, S. Glenzer, D. G. Hicks, O. L. Landen, R. London, A. Mackinnon, N. Meezan, R. R. Prasad, J. Ralph, M. Richardson, J. R. Rygg, S. Sepke, S. Weber, R. Zacharias, E. Moses, J. Kilkenny, A. Nikroo, T. C. Sangster, V. Glebov, C. Stoeckl, R. Olson, R. J. Leeper, J. Kline, G. Kyrala, and D. Wilson, Rev. Sci. Instrum. **83**, 10D901 (2012).

[11]F. H. Seguin, N. Sinenian, M. Rosenberg, A. Zylstra, M. J.-E. Manuel, H. Sio, C. Waugh, H. G. Rinderknecht, M. G. Johnson, J. Frenje, C. K. Li, R. Petrasso, T. C. Sangster, and S. Roberts, Rev. Sci. Instrum. **83**, 10D908 (2012).

[12]M. J. Rosenberg, A. B. Zylstra, J. A. Frenje, H. G. Rinderknecht, M. G. Johnson, C. J. Waugh, F. H. Séguin, H. Sio, N. Sinenian, C. K. Li, R. D. Petrasso, V. Y. Glebov, M. Hohenberger, C. Stoeckl, T. C. Sangster, C. B. Yeamans, S. LePape, A. J. Mackinnon, R. M. Bionta, B. Talison, D. T. Casey, O. L. Landen, M. J. Moran, R. A. Zacharias, J. D. Kilkenny, and A. Nikroo, Rev. Sci. Instrum. **85**, 103504 (2014).

[13]M. G. Johnson, J. A. Frenje, D. T. Casey, C. K. Li, F. H. Séguin, R. Petrasso, R. Ashabranner, R. M. Bionta, D. L. Bleuel, E. J. Bond, J. A. Caggiano, A. Carpenter, C. J. Cerjan, T. J. Clancy, T. Doeppner, M. J. Eckart, M. J. Edwards, S. Friedrich, S. H. Glenzer, S. W. Haan, E. P. Hartouni, R. Hatarik, S. P. Hatchett, O. S. Jones, G. Kyrala, S. L. Pape, R. A. Lerche, O. L. Landen, T. Ma, A. J. MacKinnon, M. A. McKernan, M. J. Moran, E. Moses, D. H. Munro, J. McNaney, H. S. Park, J. Ralph, B. Remington, J. R. Rygg, S. M. Sepke, V. Smalyuk, B. Spears, P. T. Springer, C. B. Yeamans, M. Farrell, D. Jasion, J. D. Kilkenny, A. Nikroo, R. Paguio, J. P. Knauer, V. Y. Glebov, T. C. Sangster, R. Betti, C. Stoeckl, J. Magoon, M. J. Shoup III, G. P. Grim, J. Kline, G. L. Morgan, T. J. Murphy, R. J. Leeper, C. L. Ruiz, G. W. Cooper, and A. J. Nelson, Rev. Sci. Instrum. **83**, 10D308 (2012).

[14]B. Lahmann, M. G. Johnson, J. A. Frenje, Y. Y. Glebov, H. G. Rinderknecht, F. H. Séguin, G. Sutcliffe, and R. D. Petrasso, Rev. Sci. Instrum. **91**, 053502 (2020).

[15]J. F. Ziegler, J. P. Biersack, and M. D. Ziegler, *The Stopping and Range of Ions in Matter* (SRIM Company, 2015).

[16]C. Werner, MCNP Users Manual - Code Version 6.2, Report LA-UR-17–29981, Los Alamos National Laboratory, 2017.

[17]N. Sinenian, M. J.-E. Manuel, A. B. Zylstra, M. Rosenberg, C. J. Waugh, H. G. Rinderknecht, D. T. Casey, H. Sio, J. K. Ruszczynski, L. Zhou, M. G. Johnson, J. A. Frenje, F. H. Séguin, C. K. Li, R. D. Petrasso, C. L. Ruiz, and R. J. Leeper, Rev. Sci. Instrum. **83**, 043502 (2012).